A New Topology of PV-Linked Grid-Connected Modular Multi-level Converter Based on Current-fed Quadruple-Active Bridge Converter

Mohammad Jafari[*] , Zahra Malekjamshidi

School of Electrical and Data Engineering, University of Technology Sydney, NSW, 2007, Australia
[*]mohammad.jafari@uts.edu.au

Abstract: This paper proposes a new topology of modular multi-level converter (MMC) based on current-fed quadruple active bridge (CFQAB) converter for grid integration of photovoltaic (PV) systems. The MMC tpology includes multiple cascaded converter modules in each phase of a three phase system. Each individual module is further formed by a PV-linked CFQAB dc-dc converter to integrate the PV outputs and supply it to a high-voltage dc (HVDC) bus and further to a cascaded inverter to converter to the ac voltage for distribution grid. The proposed topology features a wide input voltage range, lower current ripple and smaller size due to use of CFQAB converter as the building block which makes it an ideal choice for PV applications. The operation principle of the MMC, converter modules and the control techniques have been presented in details. A scale-down prototype of the topology is implemented to validate the operation of the proposed topology and the control systems.

1. Introduction

Incrasing global energy crises, energy demand and enviromental concerns from conventional fossil fuels have been increasing interest in the renewable energy systems over the past decades [1]. Meanwhile, photovoltaic (PV) renewable energy systems attracted more attention due to the continuous improvement in their performance and reduction of the installation cost [2]. Besides the small scale rooftop PV systems, medium to large scale solar energy systems have been developed over the past decade. However, effective integration of these low-voltage (LV) systems into the medium voltage (MV) distribution grids still remain a challenge and attractive research interest [3]. Modular multi-level converters (MMCs) have been the most feasible topology for this application so far [2], [3]. The main advantage of these topologies is utilizing low rating switching components for high voltage applications which leads to higher reliability, modularity and redundancy. Furthermore, galvanic isolation and compact size can be achieved due to the use of high-frequency transformer instead of low-frequecy bulky ones [4]. Other advantages are lower generated harmonics and electromagnetic interference and high compatibility with the smart-grid control techniques [4], [5]. A typical topology of a PV-linked MMC contains multiple dc-ac converter modules connected in series to form each phase of the three-phase system. Each module includes a dc-dc converter to boost the output voltage of the PV panels and maintain the maximum power point tracking (MPPT) followed by a grid-connected single-phase cascaded inverter [5]. Dual active bridge (DAB) topology has been widely used at the dc-dc conversion stage due to the simple structure and control, soft-switching and capability and high efficiency [4], [6]. It has been used as a building block in the dc-dc conversion stage of the modular smart transformers [7]. The DAB converter topology includes two full-bridge dc-ac conversion cells linked to a high-frequency transformer and a bidirectional power flow can be achieved by applying a phase shift angle between the generated squarewaves at the primary and secondary side of the transformer [8]. The topology can be further extended to the multi-active bridge (MAB) converter by connecting more active bridges to a multi-winding transformer (MWT) [8], [9]. The resultant topology leads to a reduced number of conversion cells and transformers which leads to a further reduction of the size and cost of the system, while still preserves the same advantages [10]. In this case, the MWT operates as a common magnetic bus to integrate the energies in the form of magnetic flux [11]-[13]. The power flow in the MWT is controlled by a phase shift control technique [9]-[13]. The most common topologies of the MAB converter are triple-active bridge (TAB) [12], and quadruple-active bridge (QAB) [13]. However, increasing the number of bridges and transformer windings to more than four leads to the complexity in the structure and design of MWT [14], [15]. A current-fed half-bridge conversion cell is proposed in [16] for high power PV-linked converters to reduce the size and cost of the system. However, start-up circuits are required to control the converter at the starting time as the duty cycle in this topology can never be less than 50 % [4]. A topology of PV-linked MMC based on the DAB converter is proposed in [17]. However, the topology can be further simplified by combining the DAB converters into the MAB configuration as has been suggested in this paper.

In the case of PV-lined converter modules, several factors such as generated current ripple, operating input voltage range and MPPT capability need to be considered. Due to the intermittent nature of irradiation level and temperature, the maximum power extracted from a PV port is variable and depends on climatological conditions [18]. Therefore, the conversion cell should be able to maintain the maximum power point tracking (MPPT) of the PV panel [19]. On the other hand, the PV output voltage level is low and needs to be boosted before applying to the inverter stage. The selected topology also should generate minimum current ripple on the PV output as high current ripple deteriorates the MPPT performance and the PV panel efficiency [20],[21]. The boost dc-dc converters have been conventionally used to step up the PV output voltage and realize the MPPT [22], [23]. However, a dc-ac converter is still required to link the PV output to the MWT.
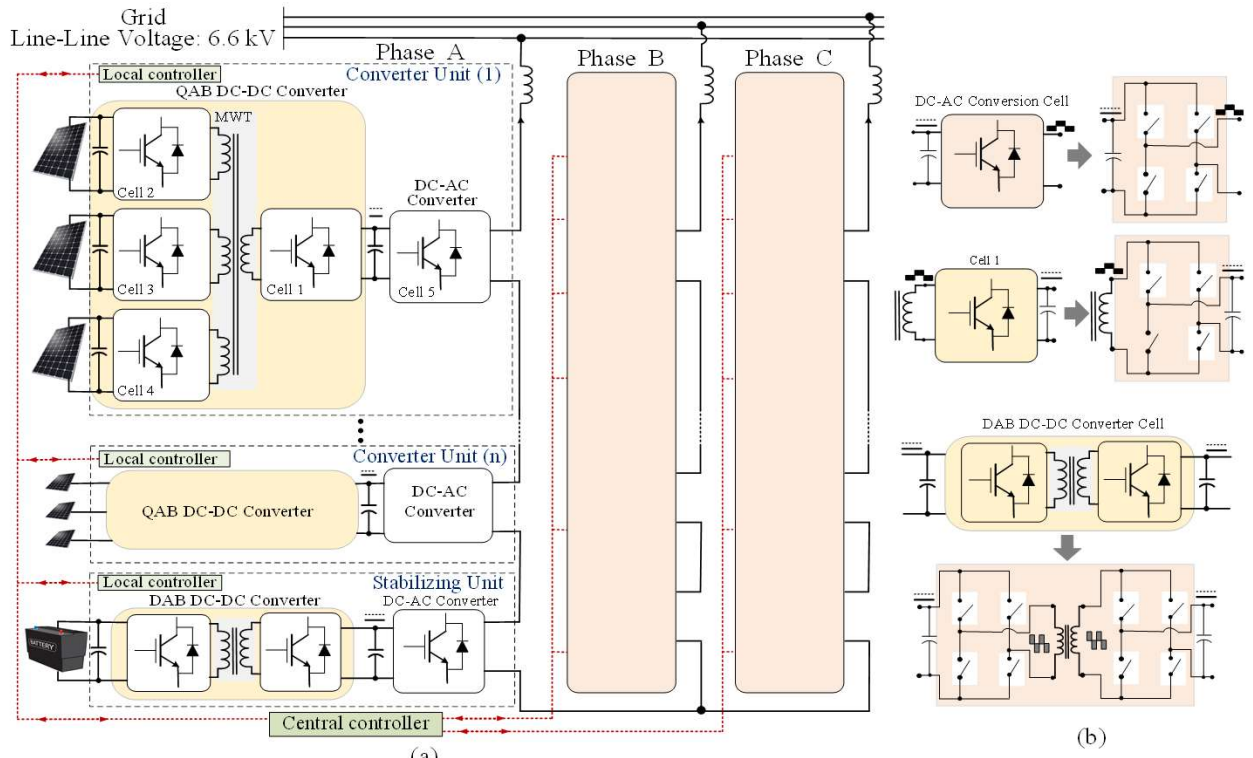
Fig.1. (a) Structure of the proposed modular multi-level converter and (b) detailed schematic of each conversion cell

In this paper, a new topology of a PV-linked grid-connected MMC is proposed as presented in Fig.1. As can be seen, each phase of the converter includes a series connection of multiple converter modules and each module includes a QAB dc-dc converter (could be a TAB topology) followed by a cascaded single- phase inverter. By using QAB topology, four active bridges are connected to the MWT. This reduces the number of conversion cells and transformers, and consequently the size and cost of the entire system in contrast to the conventional DAB converter based modules, while still preserves the same advantages. Furthermore, using current-fed full-bridge (CFFB) topology in the PV-linked cells (cell 2,3 and 4) reduces the generated ripple and extends the operating voltage range on the PV outputs. As a further contribution, several control techniques have been employed to improve the performance of the converter modules. A synchronized voltage balance (SVB) technique is used to reduce the root-mean-square (RMS) and the peak value of currents in the windings of the transformer and switching devices and improve the converter efficiency. A resonant-proportional-integral (PIR) compensator is used in the control system to reduce the low-frequency (2ω) ripple propagated from inverter output on the PV output and improve the MPPT performance.

The rest of the paper is organized as follows. The steady-state operation and some design considerations of the proposed MMC are discussed in section 2. The control systems design have been presented in section 3. The experimental test results are presented in section 4. Conclusions are derived in section 5.

2. Steady State Operation

Structure of the proposed MMC topology is presented in Fig.1. As can be seen the MMC topology includes a three-phase star connected system each phase includes n series connected dc-ac converter modules. Each module includes a PV-linked QAB dc-dc converter followed by a grid-connected single-phase inverter. Three CFFB conversion cells presented as cell 2, 3 and 4, are used in the QAB converter to boost the PV outputs at the low-voltage side (LVS) and further to the high-voltage side (HVS) and inverter.

Each PV-linked cell can be modelled as the interleaved boost converters cascaded by a voltage source full bridge dc to ac converter as presented in Fig.2. The full bridge switches S_1, S_2, S_3 and S_4 have been shared in both converters and C_2 is used as an energy buffer between the two conversion stages. The PV voltage is boosted by the interleaved converters and the extracted PV power is sent to C_2 and LVS. The conversion cell should be designed to operate in continuous conduction mode (CCM) for the whole operation range. This minimizes the ripples on the current derived from the PV panel due to the interleaving effect. To realize the MPPT, the duty ratio of S_3 and S_4 is changed according to the MPPT algorithm to adjust the output voltage from PV (V_{PV}) on the desired value. The full bridge dc-ac converter then changes V_{LVDC} to a rectangular high-frequency voltage (v_{t2}) linked to the transformer winding. The relation between the duty cycle of S_3 or S_4 (presented as D) and duty cycle of v_t (presented as D') is defined as

$$D' = \begin{cases} 2D & D <= 0.5 \\ 2(1-D) & D >= 0.5 \end{cases} \quad (1)$$

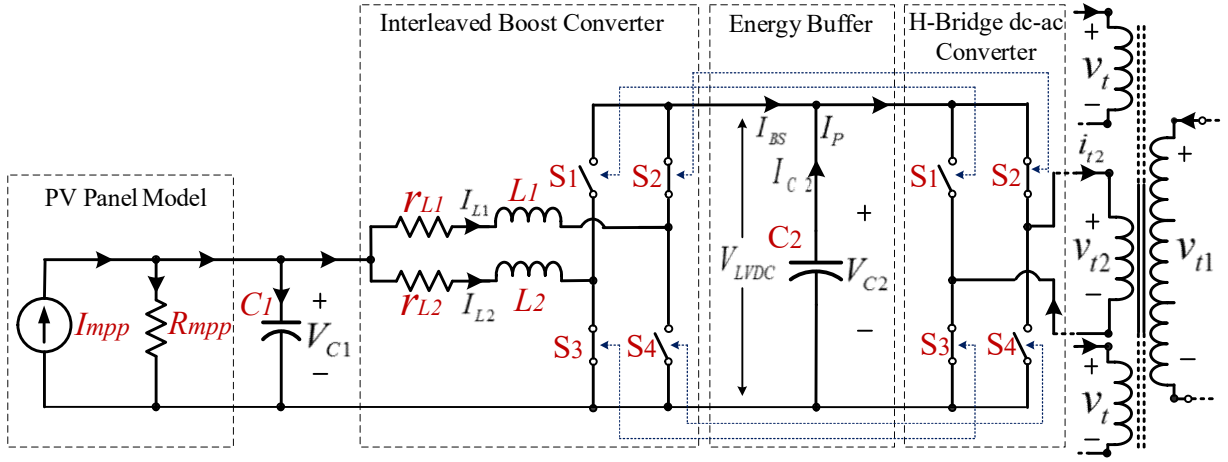On the other hand, a square wave voltage (v_{t1}) with the same frequency is generated from the at the HVS (V_{HVDC})

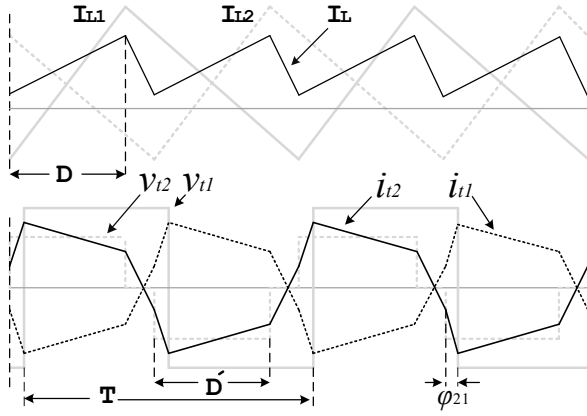Fig.2. The equivalent circuit of the PV-linked CFFB conversion cell

Fig.3. The waveforms of the conversion unit

Fig.4. Equivalent model of a PV-linked conversion cell for ZVS analysis

achieve higher efficiency [4].

2.1 Soft-switching operation

by full bridge in cell 1. Fig.3 shows the waveforms of the voltage and current in the CFFB conversion cell where D=0.4, D'=0.8, and φ_{21} =π/6. The waveforms of other conversion cells are similar assuming almost similar irradiation and temperature for all PV panels connected to the same converter unit. The power flow between the PV-linked conversion cell "X" (where X=2, 3 and 4) to cell 1 presented as P_{X1} is controlled by a leading phase-sift φ_{X1} and can be calculated from [34]

$$P_{X1} = \frac{V_{HVDC}V_{LVDC}}{2\pi^2 f_s n_{X1}(L_X+L_1')}\begin{bmatrix} \phi_{X1}(\pi - \phi_{X1}) \\ -0.25\pi^2(1 - D')^2 \end{bmatrix} \quad (2)$$

where V_{HVDC} ,f_s, L_X and L'_1 are respectively the dc voltage at the HVS, switching frequency, the leakage inductance of the transformer winding linked to the conversion cell "X" and the referred value of leakage inductance of the winding in cell 1. Furthermore, $n_{X1}=N_X/N_1$ represents the turns ratio of winding X to one. As D is changed independently according to the MPPT requirement, D' is dependent on D and cannot be used to control the power flow. Therefore, the phase shift angle (φ_{X1}) is used as another degree of freedom to regulate V_{LVDC} on the desired value and also control the power flow between the PV-linked cells and cell 1. The operation modes of the QAB converter depends on the variation range of duty ratio D (from 0 to 1) and phase shift angle φ (from 0 to π). In the proposed converter the practical phase shift angle is less than π/2, and the duty cycle, D, is changed around 0.5 to
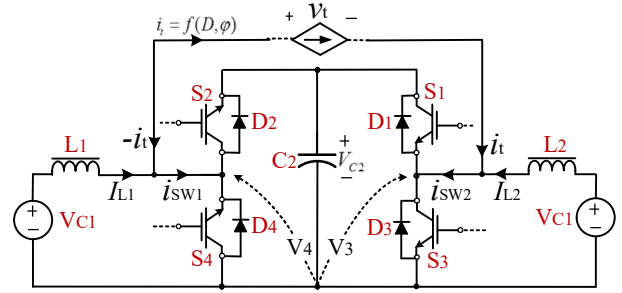
The ZVS operation mode of a conversion cell is in a limited range although, in the case of equal volt-second for all windings of the magnetic link, ZVS operation is guaranteed. This increases the ZVS operation range of the QAB converter and minimizes the RMS and peak current and consequently the conduction loss in the transformer windings and switching devices [17]. However, the current in the transformer winding depends only on the applied square wave voltages at the LVS and HVS and the ZVS condition is achievable at the HVS as long as the SVB rule is satisfied. The condition at the low-voltage side (LVS) is more complex as the current in the switching devices also depends on the current in the interleaved inductors L_1 and L_2. Fig.4 shows a simplified equivalent model of the PV linked cell in the QAB converter. According to the presented currents, the ZVS can be realized when the following conditions are achieved.

ZVS Condition
$$I_{SW1} = I_{L1} - i_t \Rightarrow$$
$$I_{SW2} = I_{L2} + i_t$$
$$\begin{cases} I_{SW1}(t_1) > 0, I_{L1} > i_t & when\ S_2 \to ON, S_4 \to OFF \\ I_{SW1}(t_4) < 0, I_{L1} < i_t & when\ S_2 \to OFF, S_4 \to ON \\ I_{SW2}(t_3) > 0, I_{L2} > -i_t & when\ S_1 \to ON, S_3 \to OFF \\ I_{SW2}(t_2) < 0, I_{L2} < -i_t & when\ S_1 \to OFF, S_3 \to ON \end{cases} \quad (3)$$

The above condition is only applicable to the Boost operation mode however, the ZVS conditions are symmetrical for both Boost and Buck modes. The current directions in the LVS have been presented in Fig.4. As can be seen the conditions

presented in (3) is achieved for a complete range of operation as long as the SVB rule is satisfied. In the proposed QAB converter, all three PV-linked ports at LVS are controlled to operate with the same phase shift angle respected to the HVS for the same PV generation to minimize the circulating power between the LVS ports. The reference voltage at LVS is also selected according to the SVB rule. However, in the case of different PV generation, the ZVS operation range is poorly achieved and needs more complicated analysis as presented in [24]. To minimize the RMS and peak current and consequently the conduction loss in the transformer winding and guarantee a full range of ZVS operation for all conversion cells, the volt-second product on all windings of the MWT should be kept equal [4], [25]. Therefore, V_{LVDC} is adjusted according to the V_{HVDC} level at the inverter side and is known as SVB) technique. The reference voltage for the LVDC bus in the cell X ($V_{LVDC,X}^*$) is defined from

$$V_{LVDC,X}^* = \frac{n_{X1}}{D} V_{HVDC} \qquad (4)$$

The capacitor C_2 is used as an energy storage component and buffer between two conversion stages. However, it needs to be selected properly to cancel out the low-frequency (2ω) voltage ripples reflected from the inverter output on the HVDC bus and the PV output.

2.2 Maximum power point tracking of the PV panels

The output voltage of the PV panels does not change in a wide range due to the irradiation and temperature levels and the main effect is on the output current. Therefore, the maximum power point (MPP) is changing in the PV panel which needs to be tracked accordingly using an appropriate MPPT algorithm. An efficient MPPT method should provide a fast and accurate tracking response with minimum oscillations around the steady-state operating point for a wide range of variations in the solar irradiation and temperature levels. Therefore, a large number of MPPT algorithm can be found in the literature [26]. In this paper, the incremental conductance (INC) method is used due to the accuracy and minimum effects on the PV operating point. To improve the dynamic response of the method a variable step size algorithm is employed [26]. The step size is automatically adjusted according to the distance between the current operation point and maximum power point. The step size increases when the operating point is far from MPP, and it decreases when the operation point is near to the MPP. The steps are applied directly to the duty ratio of the interleaved converter to adjust the output voltage of the PV on the MPP voltage (V_{mpp}). Each step change in duty ratio is calculated by the voltage and power of the PV port at k and k-1 sampling times from

$$D^*(k) = D^*(k-1) \pm N(k) \left| \frac{P(k)-P(k-1)}{V(k)-V(k-1)} \right| \qquad (5)$$

where $N(k)$ is the scaling factor that is used to adjust the step size efficiently and P(k)=$V(k)*I(k)$ the PV power at the sampling time k.

2.3 Design of high-frequency multi-winding transformer

The high-frequency MWT plays an important role in the QAB converter, the modul efficiency and entire MMC due to the modular structure. It should be designed properly to present similar characteristics for all PV-linked conversion cells to minimize the cross-coupling effects. As leakage inductance of the transformer windings is used as energy transfer elements, the PV-linked windings W2, W3 and W4 should present the same leakage inductance and also mutual inductance to the W1 at the HVS. On the other hand, the transformer efficiency considering core and copper loss analysis should be carefully considered in the design procedure. Therefore, design and development of the MWT requires extra attention. To design the transformer core, different magnetic materials have been considered. The soft ferrites present low flux density (0.3-0.5 T) which lead to a larger size transformer and higher core and copper loss. In contrast, Amorphous alloy and Nanocrystalline materials have high saturation flux density, high permeability, and low core loss. However, Nanocrystalline materials have presented lower core loss than the amorphous alloys although their saturation flux density (0.8–1 T) is much lower than that of amorphous alloys (1.4– 1.6 T) [14],[15]. Finally, the Metglas amorphous alloy (2605SA1) made by Hitachi metals has been selected considering maximum flux density, specific core loss, cost and suitability for design of toroidal cores (available in strip of 25-mm width and 20-μm thickness). The toroidal shape was selected for the magnetic core in contrast to E and U shaped cores as it provides more flexibility in the magnetic core design using thin tapes of Amorphous materials. Furthermore, achieving a symmetrical distribution of windings with the similar characteristics for all three conversion cells is possible. The design procedure is divided into three stages to provide the reasonable accuracy and computational effort as is presented in more details in [14].

The process started with a primary design stage where the transformer dimension including the core dimension and number of turns were calculated using classical equations considering transformer parameters as bulk elements [14]. The resultant magnetic structure then was used as an initial design point for the second stage which was an iterative numerical modelling based on the reluctance network modelling (RNM) [15]. At this stage the resultant structure was divided into thousands of tiny 3D magnetic elements modelled by a network of equivalent electrical circuits and is analysed using ordinary electrical equations. The calculation domains have been changed iteratively to find the best dimension with satisfactory loss and thermal conditions [15]. In this paper, the toroidal core thickness (d_w), core average radius (r_w) and the basic number of windings turn (N_w) are selected as the main variables and have been changed in a predefined range around the primary design point. Using RNM reduces the calculation efforts due the iterations in contrast to the finite element method (FEM). The resultant structure finally is analysed using FEM for a more accurate calculation of the magnetic field distribution, transformer characteristics and core dimension. Fig.5 shows more details about the FEM analysis of flux distribution associated to W2 in the magnetic core, physical dimension and experimentally developed transformer. The Litz wires have been used to reduce the skin and proximity effects due to the high-frequency currents [14],[15]. As can be seen, winding one (W1) is divided into three sections distributed around the magnetic core symmetrically. The windings of the PV-linked conversion cells (W2, W3 and W4) have similar number of turns, winding length and physical situation respected to W1 to present similar leakage inductance and mutual inductance to W1. To validate the designed transformer under the square wave excitation, the frequency response of the transformer
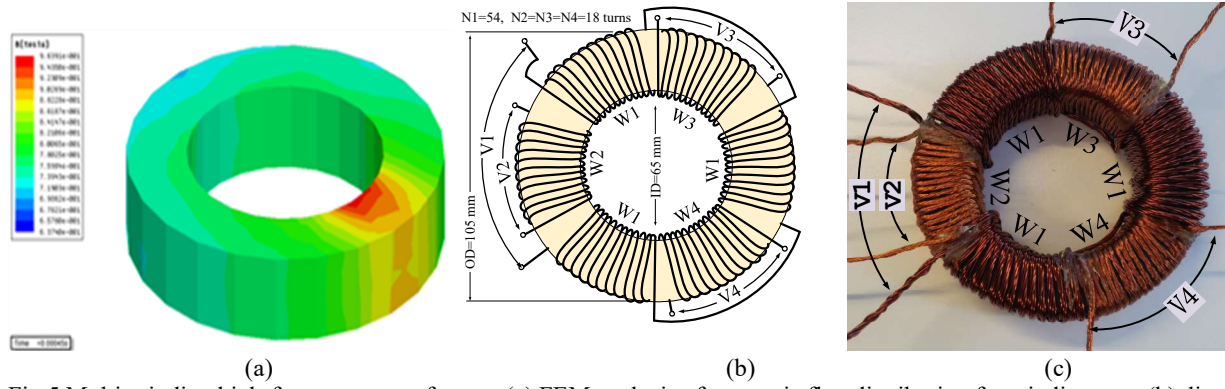
Fig.5 Multi-winding high-frequency transformer, (a) FEM analysis of magnetic flux distribution for winding two, (b) dimension and windings distribution, and (c) experimentally developed structure.
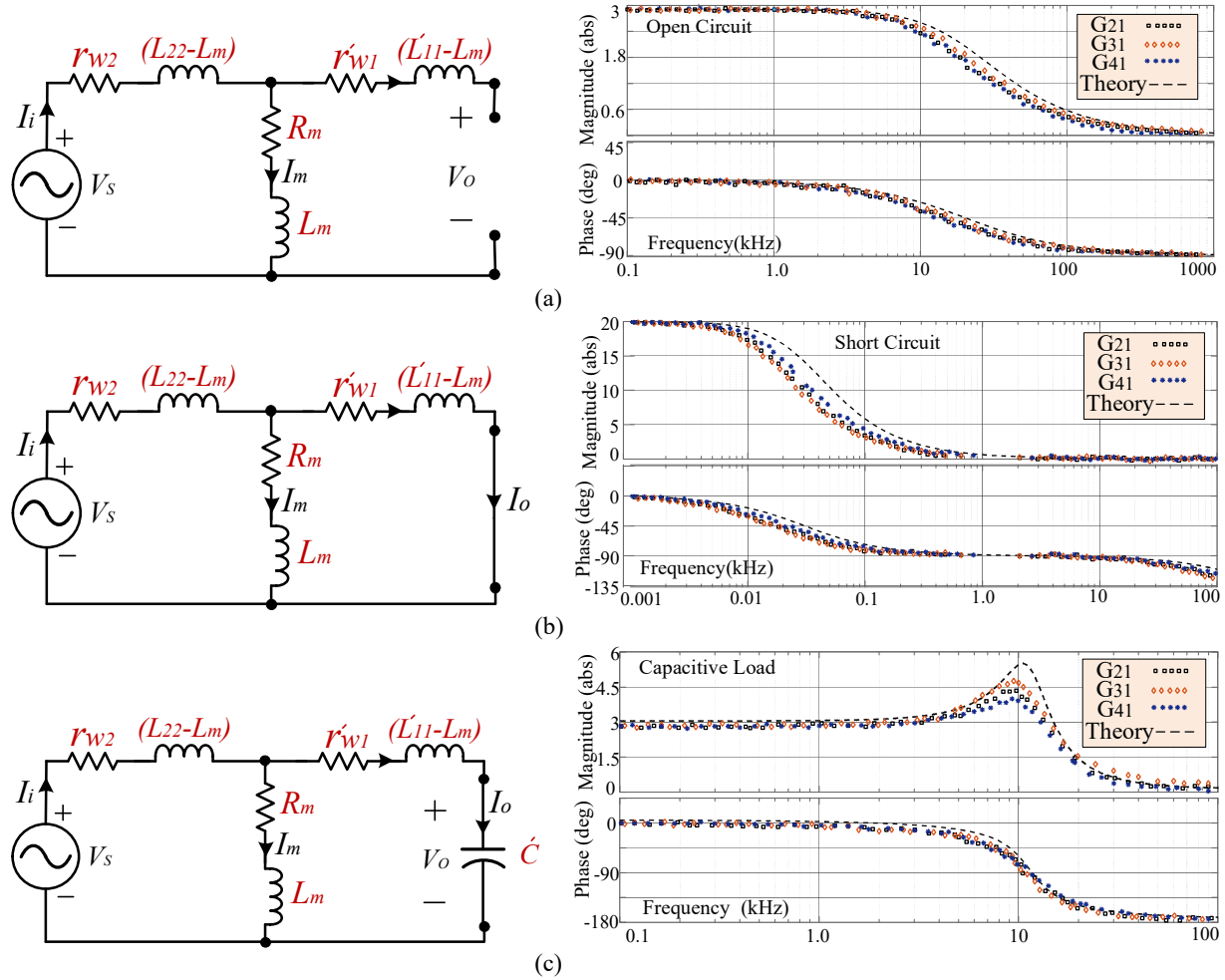

Fig.6. The experimental test of the multi-winding transformer and frequency response for (a) open circuit test, (b) short circuit test and (c) capacitive load

model based on the parameters found from numerical analysis and the experimentally developed transformer have been compared for three cases of open circuit, short circuit and capacitive load. This indicates the difference between characteristics of the windings W2, W3 and W4 for a wide range of frequency and also their adaptation to the numerically obtained results. The excitation voltage with variable frequency was applied to winding two, three and four and the output signal is collected from winding one. The magnetizing

inductance (L_m) and the equivalent core loss resistance (R_m) are replaced by their equivalent series elements as presented in Fig.6 [14], [15]. The output to input transfer function in the case of open circuit when excitation is applied to W2 and output voltage collected from W1 can be written as

$$\frac{V_O}{V_S} = \frac{R_m + SL_m}{r_{W1} + R_m + SL_{22}} \tag{6}$$

where r_w, L_{11} and L_{22} are the winding resistance, self-inductance of winding one and winding two respectively.

In the case of short circuit the transfer function can be written as

$$\frac{I_O}{V_S} = \frac{Z}{[r_{W2} + (L_{22} - L_m)S + Z][r'_{W1} + (L'_{11} - L_m)S]}$$

$$[Z]^{-1} = [R_m + SL_m]^{-1} + [r'_{W1} + S(L'_{11} - L_m)]^{-1} \qquad (7)$$

and for the capacitive load, the transfer function is

$$\frac{V_O}{V_S}$$

$$= \frac{Z}{[r_{W2} + (L_{22} - L_m)S + Z][1 + SC'r'_{W1} + S^2 C'(L'_{11} - L_m)]}$$

$$[Z]^{-1} = [R_m + SL_m]^{-1} + [r'_{W1} + S(L'_{11} - L_m) + 1/SC']^{-1} \qquad (8)$$

As can be seen in Fig.6, the frequency response of the prototype transformer for all three windings adapts to the numerically calculated model. Furthermore, all three windings presented the same frequency response to winding one due to the designed symmetrical structure and similar characteristics. The frequency range of 10kHz to 100 kHz is selected based on the switching frequency (principal harmonic), 1st, 2nd, 3rd, 4th, and 5th harmonics of the current waveforms to model the actual operating condition when phase-shifted square wave voltage is applied to the windings.

3. Design of the Control System

The control system of the proposed MMC includes the local controllers of each converter module and a master controller which controls the entire MMC and mmunicates to the network control center. This section presents analysis and design of the local controller of each converter module only and detail of the master controller operation remains for future publication. Each local controller includes an MPPT control system to maximize the PV output powers, a power flow control system in the QAB converter, and a direct current control loop for the single-phase inverter as will be discussed in the following sections.

3.1. Design of the PV output controller

As presented in Fig.2, each PV-linked CFFB conversion cell can be decomposed into the interleaved boost converter followed by a voltage source full-bridge dc-ac converter. To adjust the PV operation point on the MPP, the output voltage V_{C1} should be adjusted accurately according to the MPPT algorithm requirements. The design procedure of the interleaved converter is carried out for a single leg due to the similarity of components and operation principles of two boost converters. To design the controller, a small signal model of the conversion cell is required. As presented in Fig.2, the PV panel is modeled with the Thevenin equivalent circuit at the operation point due to the slow dynamic response of the PV [4]. The equivalent resistor R_{mpp} can be calculated from $R_{mpp} = V_{mpp}/I_{mpp}$ where V_{mpp} and I_{mpp} are the PV panel output voltage and output current at the MPP respectively.

To design a more robust controller for adjusting the PV voltage on MPP, a dual loop control system including inner inductor current and outer PV voltage control loops is proposed. To design the controller, the transfer function of the PV output voltage as the control output to the inductor current as the control input is required. The average state equation of the PV voltage based on the inductor current can be written as

$$C_1 \frac{dV_{C1}}{dt} + I_L + \frac{V_{C1}}{R_{mpp}} - I_{mpp} = 0 \qquad (9)$$

Adding small signal variations to the equation and considering only the ac elements, the equation can be rewritten as

$$C_1 \frac{d\hat{v}_{C1}}{dt} + \hat{\imath}_L + \frac{\hat{v}_{C1}}{R_{mpp}} = 0 \qquad (10)$$

The transfer function of the PV voltage to the inductor current then can be determined using the Laplace transform of (10) as

$$G_{v-PV} = \frac{V_{C1}(s)}{I_L(s)} = \frac{-R_{mpp}}{1 + sC_1 R_{mpp}} \qquad (11)$$

On the other hand, the state space equations for inductor current over a complete switching cycle can be written as

$$\begin{cases} L_2 \frac{dI_L}{dt} = V_{C1} - I_L r_L & 0 < t < DT \\ L_2 \frac{dI_L}{dt} = V_{C1} - I_L r_L - V_{C2} & DT < t < T \end{cases} \qquad (12)$$

The final equation by averaging (12) over a complete operating cycle is obtained as

$$L_2 \frac{dI_L}{dt} = V_{C1} - I_L r_L - (1 - D)V_{C2} \qquad (13)$$

Adding the small signal variations and taking Laplace transform, results in the following equation for the inductor current.

$$I_L(s) = G_{i-V} V_{C2}(s) - G_{i-D} D(s) \qquad (14)$$

where G_{i-V} and G_{i-D} are the transfer functions of the voltage at LVS (V_{C2}) and the duty cycle (D) to the inductor current respectively and are defined from

$$G_{i-V} = \frac{V_{C2}(s)}{I_L(s)} = \frac{-D}{sL_2 + r_L}, \ G_{i-D} = \frac{D(s)}{I_L(s)} = -\frac{V_{C2}}{sL_2 + r_L} \qquad (15)$$

Fig.7 shows the designed dual loop control system. The bandwidth of the inner current control loop should be selected much higher than that of the PV voltage control loop. Therefore, a low-bandwidth control loop with more robustness and stability can be used for PV voltage control. The control blocks $H_1(s)$ and $H_2(s)$ are the transfer functions of low-pass first-order filters that filter out the high-frequency components of the PV voltage and inductor current respectively and are defined as

$$H_1(s) = \frac{K_{f1}}{1 + \tau_1 s}, H_2(s) = \frac{K_{f2}}{1 + \tau_2 s} \qquad (16)$$

where $\tau_1 = 0.95$ ms and $\tau_2 = 0.5$ ms are the time constants of the filters. The feedback gains of K_{f1} and K_{f2} are selected according to the signal conditioning circuit parameters. The compensator blocks C_{v-PV} and C_{i-PV} are the proportional-integral (PI) controller transfer functions of the voltage and current control loops respectively and can be presented in the general form as

$$C(s) = K_P + \frac{K_I}{s} \qquad (17)$$

where the proportional (K_P) and the integral (K_I) gains are determined based on the required crossover frequency (ω_c) and the phase margin (φ_m) of the voltage and current control loops [27], [28]. Assuming that the PI controller transfer function is given as

$$C(j\omega) = K_P + \frac{K_I}{j\omega} = K_P - j\frac{K_I}{\omega}$$

$$|C(j\omega)| \angle \theta = |C(j\omega)|[(cos(\theta) + j\,sin(\theta)] \qquad (18)$$

Then the design problem is to find K_P and K_I for a chosen crossover frequency (ω_c) and phase margin (φ_m) such that

$$C(j\omega_c)G(j\omega_c) = 1\angle(180 + \phi_m) \qquad (19)$$
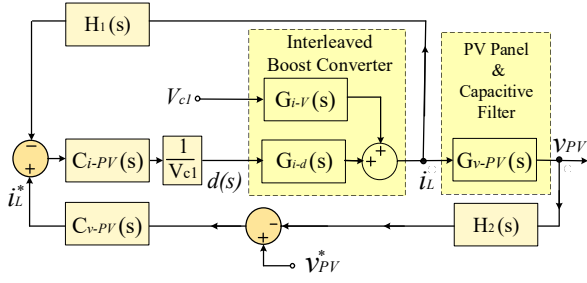
From (19), we can find the following equations

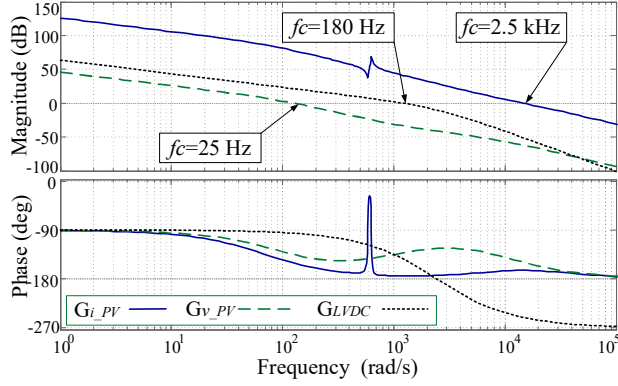Fig.7. Block diagram of the PV voltage control system

Fig.8. Magnitude and phase bode diagrams of the PV output voltage and dc bus voltage control loops

$$|C(j\omega_c)| = \frac{1}{|G(j\omega_c)|}$$

$$\angle C(j\omega_c) = \theta = 180 + \phi_m - \angle G(j\omega_c) \quad (20)$$

Finally, from (18) and (20) the values of controller coefficient can be determined as

$$K_P = |C(j\omega_c)| \cos(\theta) = \frac{\cos(\theta)}{|G(j\omega_c)|} \quad (21)$$

$$-\frac{K_I}{\omega_c} = |C(j\omega_c)| \sin(\theta) = \frac{1}{|G(j\omega_c)|} \sin(\theta)$$

$$\Rightarrow K_I = \frac{-\omega_c \sin(\theta)}{|G(j\omega_c)|} \quad (22)$$

$$\theta = 180 + \phi_m - \angle G(j\omega_c) \quad (23)$$

and $G(j\omega_c)$ is the open loop transfer function of the outer voltage or inner current control loops. The resultant transfer functions of the inductor current control (C_{i-PV}) and the PV voltage control (C_{v-PV}) are obtained as

$$C_{i-PV}(s) = 1.8 + \frac{0.003}{s} + \frac{2\omega s}{s^2 + 4\pi s + (2\omega)^2} \quad (24)$$

$$C_{v-PV}(s) = 0.1 + \frac{24.7}{s} \quad (25)$$

where $\omega = 100\pi$. As can be seen in (24), a resonant component at $\omega = 100\pi$ is added to the current control loop to increase the loop gain at $f = 50$ Hz and reduce the effect of low-frequency ripples propagated from the inverter bus [4]. This improves the stability of the PV operation point and MPPT performance. The bode diagrams of the inductor current and the PV voltage control loops are simulated for the converter unit for parameters illustrated in Table 1 and presented in Fig.8. The current loop has a crossover frequency of f_{ci}=2.5 kHz (ω_{ci}=16000 rad/s), gain margin of 60 dB and phase margin of 15°. On the other hand, the PV voltage control loop has a crossover frequency of f_{cv}=25 Hz (ω_{cv}=160 rad/s), a gain margin of 120 dB and the phase margin of 45°. Comparing the
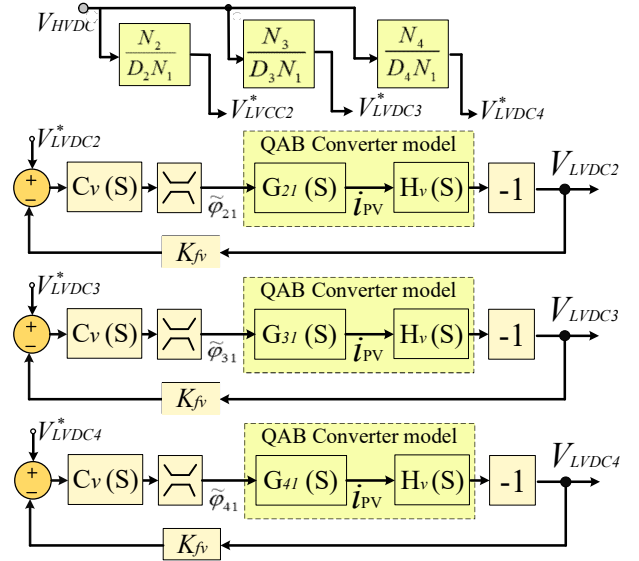

Fig.9. Block diagram of the DC bus voltage control system in the QAB converter

Table 1 The PV port parameters for small signal analysis

C_1	100 μf	V_{PV}	10-40 V	f_s	10 kHz
C_2	1200 μf	V_{LVDC}	120 V	f_{mppt}	10 Hz
r_L	300 mΩ	L_1, L_2	100 μH	K_i, K_v	0.8, 0.05

bandwidths of the voltage and current control loops shows that the current control loop has a much higher speed response compared to the voltage control loop ($f_{cv} << f_{ci}$) which means a faster reaction of the inductor current control loop.

3.2. Design of Power Flow Controller in QAB Converter

As presented in Fig.2, the conversion cell is modeled as an interleaved boost converter followed by a full bridge dc-ac converter. As the duty cycle D' is changing independently according to the MPPT requirement and is determined by D, to control the power flow from PV-linked cells (LVS) to the HVS and regulate V_{LVDC}, the phase shift angle (φ_{X1}) can be used as another degree of freedom. Fig.9 illustrates the designed control system for the voltage regulation of the LVDC bus of the PV-linked conversion cells and the power flow to the HVDC bus. As can be seen, the reference voltage of the dc bus (V^*_{LVDC}) in each of the PV-linked cells is determined according to the reference signal generated based on the SVB rule presented in (4).

The PI controllers are determined similarly to the PV output control loop. However, the required cross-over frequency and the phase margin should be designed for slower dynamic response compared to that of PV output control to avoid the interference between the control loops and undesirable oscillations and instabilities during the transient times. The amplitude and phase bode diagrams of the designed control system are presented in Fig.8. As can be seen, the cross-over frequency of the loop is about 180 Hz which is much less than that of PV output control (2.5 kHz).

3.3. Control of the cascaded inverter

The control section of the cascaded inverter in each individual module should be designed to provide proper values of the active and reactive power to the utility grid. As
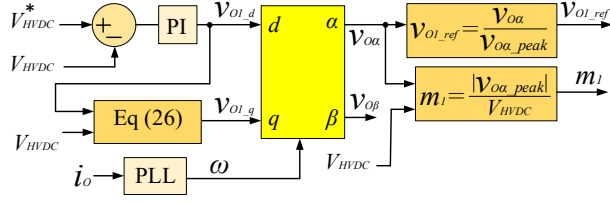
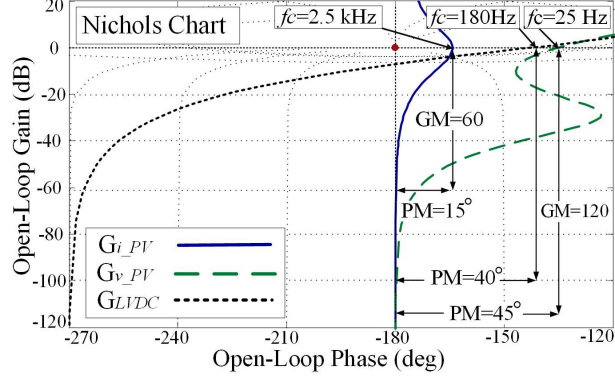Fig.10. The control scheme of bi-directional single phase inverter

Fig.11. Nichols chart including phase and gain margins of the designed control loops.

the same output current flows in the output of all cascaded modules, the active and reactive power in the output of each individual module is controlled by shifting the output voltage with respect to the current. To control the output voltage of each module, the voltage is transformed into the equivalent direct-quadrature (d-q) synchronous reference frame with respect to the output current angular speed. Therefore, the voltage elements aligned with the d-axis and q-axis determined the active and the reactive power respectively. The active power in each module is almost equal to the power generated by the linked PV panels and directly affects the V_{HVS} level. Therefore, to control the active power of each module, the difference between the V_{HVS} level and the reference value (V^*_{HVS}) is translated to the d component of the output voltage as presented in Fig.10. On the other hand, the reactive power is determined continuously by the instant value of the active power as increasing reactive power may lead to an overmodulation and distortion in the output current due to the constant value of V_{HVS}. Therefore, the available reactive component of the output voltage (V^*_{Oj-q}) in j-th converter module for each individual module is determined from

$$V^*_{Oj-} = \sqrt{V^2_{HVS} - V^2_{Oj-d}} \qquad (26)$$

where V_{Oj-d} is the d component of output voltage (active element) in j-th module. Fig.11 depicts the Nichols chart of the proposed control systems where the phase margin (PM), gain margin (GM) and cross-over frequencies are presented clearly.

4. Experimental test results

To validate the performance of the proposed PV-linked MMC, prototype is developed for a five-levels converter with two convertrer modules in each phase as presented in Fig.12.
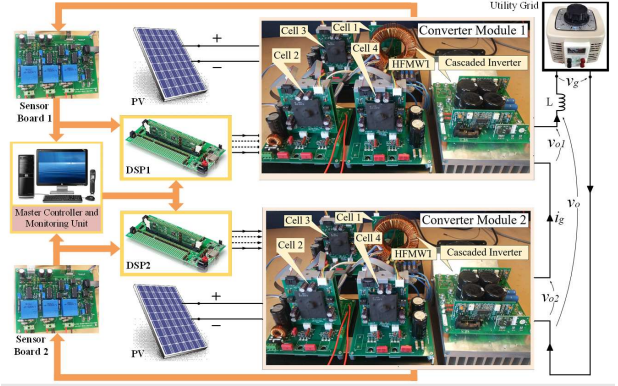

Fig.12. The experimentally developed MMC with two converter modules for one phase only
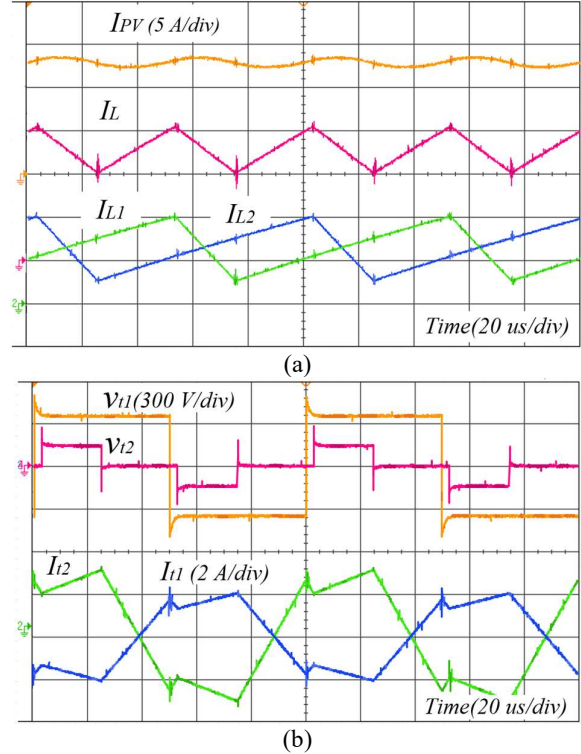

(a)

(b)

Fig.13. Experimentally measured waveforms of the interleaved boost converter and the resultant voltage and current in winding one and three of the MWT for two different operating conditions.

It includes two 4.5 kW converter module including a PV-linked QAB dc-dc converter followed by a single-phase inverter. Two DSP controllers (C2000/TMS320F28335) are used to locally control the modules and the system level control is performed by a PC using MATLAB. The voltage and current samples of all PV ports, inverter input and output are received by Hall-effect voltage (LEM/LV25-P) and current (LEM/LTSR25-NP) sensors. The MPPT process for each conversion cell is performed individually every 100 ms (f=10 Hz). The QAB converter is implemented by using IGBT switches (IKW40T120) and onboard driver integrated circuit VLA567-01R. The single-phase inverter is realized by the full bridge unit with SEMIKRON (SK30GH123) and on-board drivers.

Fig.13 shows the experimentally measured waveforms of the interleaved boost converter and the resultant voltage and
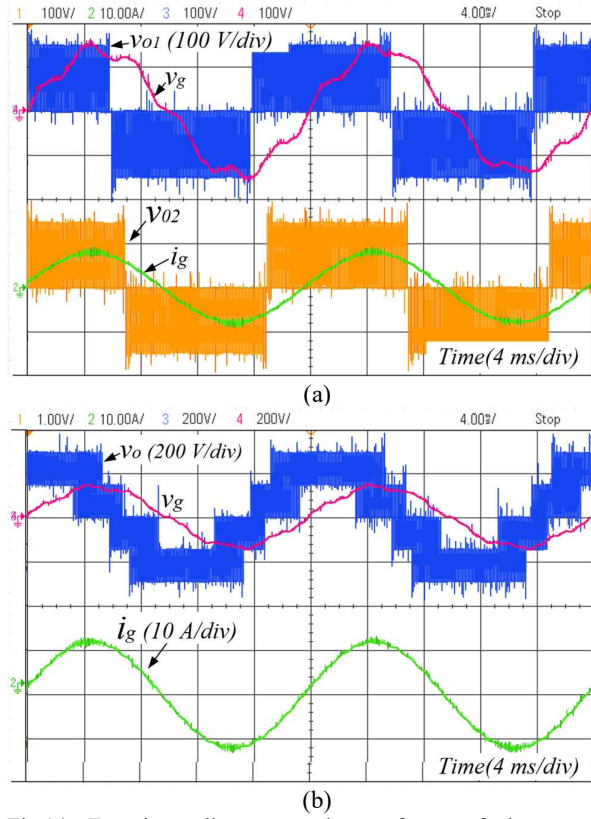
(a)

(b)

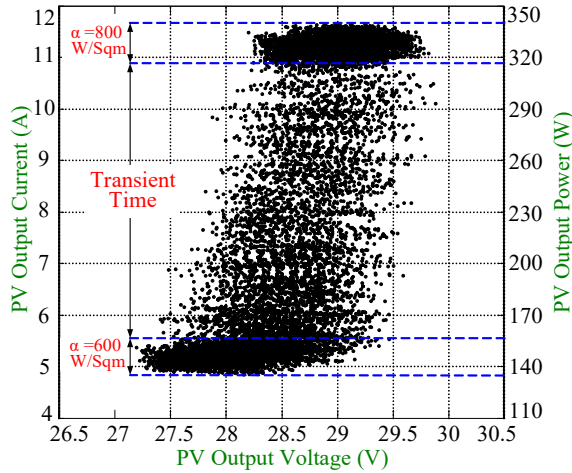Fig.14. Experimentally measured waveforms of the cascaded modules and MMC

Fig.15. Trajectory of MPPT operation for irradiation change from 600 W/sqm. to 800 W/sqm.
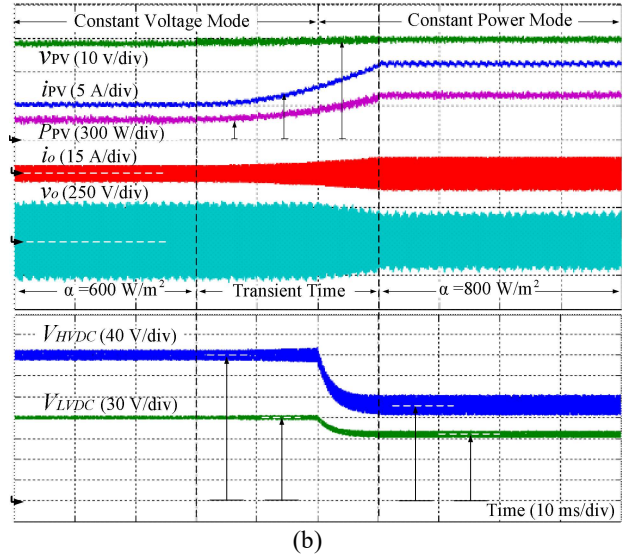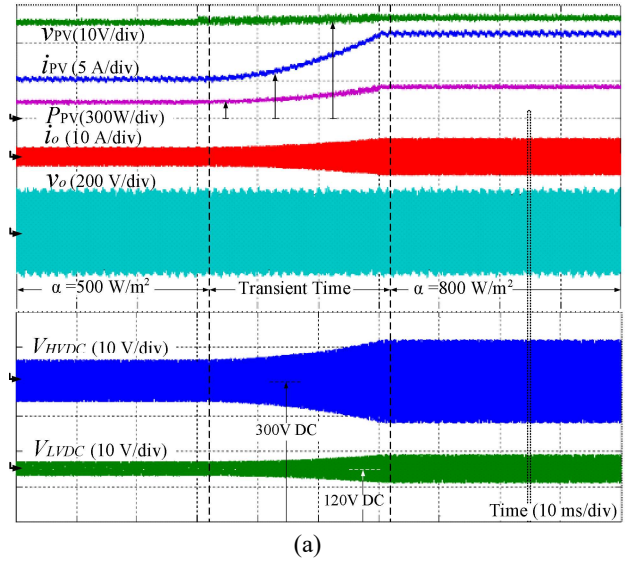

(a)

(b)

Fig.16. The dynamic response of the conversion cell against a change in the irradiation level of the PV port presenting PV voltage, current and power, the inverter output voltage and current, V_{HVDC} and V_{LVDC}. (a) from 500 W/sqm. to 800 W/sqm. (b) from 600 W/sqm. to 800 W/sqm

current in winding one and three of the MWT for two different operating conditions. The voltage and currents in ports two and four are similar to winding three due to the similarity in temperature and irradiation levels of all PV panels. Fig.14 (a) shows the experimental waveforms of two cascaded modules, and the resultant output current by MMC and also the utility grid voltage. Fig.14 (b) presents the generated five-level output voltage based on the phase-shifted carrier pulse width modulation technique and the resultant current.

To show the MPPT performance, the PV voltage and current variation during a step change in irradiation from α=500 W/m^2 to α=800 W/m^2 are recorded and presented in Fig.15. As can

be seen, the operation point of the PV closely tracks the irradiation change during transient time and the output power increases from 140 W to 350 W. Fig.16 (a) shows the dynamic response of the proposed control systems when irradiation level changes from α=500 W/m^2 to α=800 W/m^2 and a PV output power from 140W to 350W. The inverter output current increases from 5A$_{P-P}$ to 10A$_{P-P}$ due increasing PV generation while the PV output voltage remains almost constant. The voltage ripple of the HVDC and LVDC buses increases to 24 V$_{P-P}$ and 8 V$_{P-P}$ respectively. Fig.16 (b) shows similar waveforms when the irradiation level changes from 600 W/m^2 to 800 W/m^2. However, the inverter voltage drops when the output current follows the reference value provided by the master controller as PV generation is less than the expected value. The voltage ripple of the HVDC and LVDC busses follows the same trend. However, bus voltages decrease due to the generated power limit. The voltage ripple on the LVDC and HVDC buses are also presented.As can be seen, for output

ac power (P_O=1.5 kW), the voltage ripple on the HVDC and LVDC buses are about 14 V_P and 4 V_P respectively.

5. Conclusion

This paper proposed a new topology of a PV-linked grid-connected MMC based on QAB converter topology as building modules. The steady state operation of the topology was presented. Some design considerations including multi-windingvtransformer, and control techniques have been discussed in details. Operation of the proposed topology including MPPT performance, controllability and dynamic response have been experimentally tested by using a prototype to validate the suggested MMC topology.

REEFERENCES

[1]   J. Ebrahimi, E. Babaei and G. B. Gharehpetian, "A New Topology of Cascaded Multilevel Converters With Reduced Number of Components for High-Voltage Applications," *IEEE Trans. Power Elec.*, vol. 26, no. 11, pp. 3109-3118, Nov. 2011.

[2]   Dale, M.: 'Comparative Analysis of Energy Costs of Photovoltaic, Solar Thermal, and Wind Electricity Generation Technologies', Applied Science, 2013,3, pp 325-337

[3]   Xiao, B., Hang, L., Mei, J., Riley, C., Tolbert, L. M., and Ozpineci, B. : 'Modular Cascaded H-Bridge Multilevel PV Inverter With Distributed MPPT for Grid-Connected Applications', IEEE Trans. Ind. Applications, 2015, 51, 2, pp 1722-1731.

[4]   Malinowski, M., Gopakumar, K., Rodriguez, J. and Perezm, M. A., 'A Survey on Cascaded Multilevel Inverters', IEEE Trans. Ind. Electron., 2010, 57, 7, pp. 2197-2206

[5]   Rodriguez, J., Lai, J.-S. and Peng, F. Z. 'Multilevel inverters: A survey of topologies, controls, and applications' IEEE Trans. Ind. Electron., 2002, 49, 4, pp. 724–738

[6]   Liu, T. et al: 'Design and implementation of high efficiency control scheme of dual active bridge based 10kV/1MW solid state transformer for PV application' IEEE Trans. Power Electron., 2019, 34, 5, pp. 4223-4238

[7]   She, X., Huang, A. Q. and Burgos, R. : 'Review of Solid-State Transformer Technologies and Their Application in Power Distribution Systems', IEEE Journal of Emerging and Selected Topics in Power Electronics, 2013, 1, 3, pp. 186-198.

[8]   Kheraluwala, M. N., Gascoigne, R. W., Divan, D. M. and Baumann, E. D. : 'Performance characterization of a high-power dual active bridge DC-to-DC converter', IEEE Trans. Ind. Applications, 1992, 28, 6, pp. 1294-1301

[9]   Falcones,S., Ayyanar, R. and Mao, X.: 'A DC–DC Multiport-Converter-Based Solid-State Transformer Integrating Distributed Generation and Storage' IEEE Trans.Power Electron, 2013, 28, 5, pp. 2192-2203

[10] Costa, L. F., Hoffmann, F., Buticchi, G. and Liserre, M., 'Comparative Analysis of Multiple Active Bridge Converters Configurations in Modular Smart Transformer' IEEE Trans. Ind. Electron., 2019, 66, 1, pp. 191-202

[11] Jafari, M., Malekjamshidi, Z. and Zhu, J. 2019, 'Design and Development of a Multi-Winding High-Frequency Magnetic Link for Grid Integration of Residential Renewable Energy Systems', Applied Energy, 242, pp. 1209-1225.

[12] Jafari, M., Malekjamshidi, Z., and Zhu, J., 'Optimal Energy Management of a Residential-based Hybrid Renewable Energy System Using Rule-based Real-time control and 2D Dynamic Programming optimization Method', Renewable Energy, 2019, 144, pp. 254-266

[13] Costa, L. F., Buticchi, G. and Liserre, M. 'Quad-Active-Bridge DC–DC Converter as Cross-Link for Medium-Voltage Modular Inverters' IEEE Trans. Ind. Applications, 2017, 53, 2, pp. 1243-1253

[14] Jafari, M., Malekjamshidi, Z., Lei, G., Wang, T., Platt, G. and Zhu, J., 'Design and Implementation of an Amorphous High-Frequency Transformer Coupling Multiple Converters in a Smart Microgrid', IEEE Trans. Ind. Electron., 2017, 64, 2, pp. 1028-1037

[15] Jafari, M., Malekjamshidi, Z., and Zhu, J., 'Copper Loss Analysis of a Multi-winding High-frequency Transformer for a Magnetically-coupled Residential Micro-grid' IEEE Trans. Ind. Applications', 2019, 55, 1, pp. 283-297

[16] Wang, Z., Li, H. : 'An integrated three-port bidirectional dc-dc converter for PV application on a dc distribution system', IEEE Trans. Power Electron., 2013, 28, 10, pp. 4612–4624

[17] Shi, Y., Li, R., Xue, Y., Li, H. : 'Optimized Operation of Current-Fed Dual Active Bridge DC–DC Converter for PV Applications' IEEE Trans. Ind. Electron, 62, 11, pp.6986-6995

[18] Abu-Rub, H., Malinowski, M., Al-Haddad, K. : 'Photovoltaic Energy Conversion Systems', proc. IEEE Power Electronics for Renewable Energy Systems' Transportation and Industrial Applications , 2014, pp.

[19] Subudhi, B. and Pradhan, R. : 'A Comparative Study on Maximum Power Point Tracking Techniques for Photovoltaic Power Systems', IEEE Trans. Sustainable Energy, 2013, 4, 1, pp. 89-98

[20] Femia, N., Petrone, G., Spagnuolo, G. and Vitelli, M.: 'A technique for improving P&O MPPT performances of double-stage grid-connected photovoltaic systems' IEEE Trans. Ind. Electron.,2009, 56, 11, pp. 4473–4482

[21] Jiang, S., Cao, D., Li, Y. and Peng, F. Z. : 'Gird-connected boost-half bridge photoltaic microinverter system using repetitive current control and maximum power point tracking', IEEE Trans. Power Electron.,2012, 27, 11, pp. 4711–4722

[22] Ahmad, M. Agarwal, W. N. and Anand, S.: 'Online Monitoring Technique for Aluminum Electrolytic Capacitor in Solar PV-Based DC System', IEEE Trans. Ind. Electron.,2016, 63, 11, pp. 7059-7066

[23] Chandra Mouli, G. R., Schijffelen, J., Bauer, P., Zeman, M. : 'Design and Comparison of a 10kW Interleaved Boost Converter for PV Application Using Si and SiC Devices', IEEE Journal of Emerging and Selected Topics in Power Electronics, 2016, 99, pp.1-1

[24] H. Tao, J. L. Duarte, M. A. M. Hendrix, "Three-port triple-half bridge bidirectional converter with zero voltage switching," *IEEE Trans. Power Electronics,* vol. 23, no.2, pp 782–792, March 2008.

[25] Tao, H., Kotsopoulos, A., Duarte, J. L., and Hendrix, M. A. M.: 'A Soft-Switched Three-Port Bidirectional Converter for Fuel Cell and Supercapacitor Applications', proc. 36th IEEE Power Elect. Specialists Conf., Recife, 2005, pp. 2487-2493.

[26] Esram, T. and Chapman, P. L., 'Comparison of Photovoltaic Array Maximum Power Point Tracking Techniques', IEEE Trans. Energy Conversion, 2007, 22, 2, pp. 439-449

[27] Jafari, M., Malekjamshidi, Z., Lu, D. D. C., and Zhu, J.: 'Development of a Fuzzy-Logic-Based Energy Management System for a Multi-Port Multi-Operation Mode Residential Smart Micro-grid', IEEE Trans. Power Electronics, 2019, 34, 4, pp. 3283-3301

[28] C. L. Phillips and H. T. Nagle, Digital Control Systems Analysis and Design, 3rd ed. Englewood Cliffs, NJ, USA: Prentice-Hall, 1995.